Lévy Walks and Path Chaos in the Dispersal of Elongated Structures Moving across Cellular Vortical Flows

Shi-Yuan Hu[1,2] Jun-Jun Chu,[3] Michael J. Shelley,[1,4,*] and Jun Zhang[1,2,5,†]

[1]*Applied Mathematics Lab, Courant Institute of Mathematical Sciences, New York University, New York, New York 10012, USA*
[2]*Department of Physics, New York University, New York, New York 10003, USA*
[3]*School of Physics Science and Engineering, Tongji University, Shanghai 200092, China*
[4]*Center for Computational Biology, Flatiron Institute, New York, New York 10010, USA*
[5]*NYU-ECNU Institute of Physics at NYU Shanghai, Shanghai 200062, China*

In cellular vortical flows, namely arrays of counterrotating vortices, short but flexible filaments can show simple random walks through their stretch-coil interactions with flow stagnation points. Here, we study the dynamics of semirigid filaments long enough to broadly sample the vortical field. Using simulation, we find a surprising variety of long-time transport behavior—random walks, ballistic transport, and trapping—depending upon the filament's relative length and effective flexibility. Moreover, we find that filaments execute Lévy walks whose diffusion exponents generally decrease with increasing filament length, until transitioning to Brownian walks. Lyapunov exponents likewise increase with length. Even completely rigid filaments, whose dynamics is finite dimensional, show a surprising variety of transport states and chaos. Fast filament dispersal is related to an underlying geometry of "conveyor belts." Evidence for these various transport states is found in experiments using arrays of counterrotating rollers, immersed in a fluid and transporting a flexible ribbon.

Flows at low-Reynolds number (Re) are typically laminar and regular. However, chaotic or turbulent dynamics can emerge, such as by flowing through complex geometries [1], adding elastic polymers [2–4], and exploiting the hydrodynamic interactions between suspended passive particles in externally driven flows [5], or between active motile ones [6,7]. The understanding of how random and complex dynamics can emerge in simple flows at low Re is important in numerous applications [8–15].

Time-independent cellular vortical flows are simple flows with inherent characteristic scales and closed streamlines. They often arise as simplified models for flows in nature [16–18] and have been realized in different experiments [19–21]. Tracer particles in such flows simply follow closed streamlines. When the particle size is negligible compared with the characteristic flow scale, complex dynamics, such as aggregation [22] and Lévy walks [18,23,24], have been found for active particles. For passive flexible filaments, which can show complex deformations even in simple shear flow [25], complex dynamics arises differently: driven by buckling instabilities near the flow stagnation points, the filaments behave as Brownian walkers across the array [21,26,27]. The recent literature on filament dynamics is reviewed in Ref. [28].

For finite-extent filaments, transport is determined by flows sampled nonlocally along the filament, in contrast with small or compact particles. Complex and different behaviors may be generated and controlled through the coupling of flows and filaments at different length scales. In this Letter, we use experiments and a comprehensive set of numerical simulations to investigate the transport of rigid and semirigid filaments when their length L is comparable to the vortex size W in an idealized Stokesian cellular flow. In this regime, the background vortices can be viewed as "soft" scatters for the filaments and the dynamics shows similarity to billiards systems [29–31]. We construct a phase diagram that shows the rich variety of transport states possible for filaments moving across this simple low-Re flow. In particular, we find that as L/W increases, there exists a transition through Lévy walks, of generally decreasing diffusion exponents and increasing Lyapunov exponents, to Brownian walks. Lévy walks have been found in the dynamics of active elongated particles in cellular flows when $L/W \ll 1$, but arising there due to particle motility [18]. Quite remarkably, even completely rigid filaments, described by only center-of-mass (COM) position and orientation, show these varieties of random walks and chaotic motions.

Besides L and W, the dynamics of a flexible filament depends also upon its elastohydrodynamic length $l_e \sim (B/\mu U_0)^{1/3}$ [32], where B is filament rigidity, μ is fluid viscosity, and U_0 is the characteristic flow velocity. The interplay among the three length scales is captured by two dimensionless control parameters: the relative length $\gamma = L/W$ and the effective flexibility $\eta \propto (L/l_e)^3$. The filament appears to be more "flexible" when η is larger.
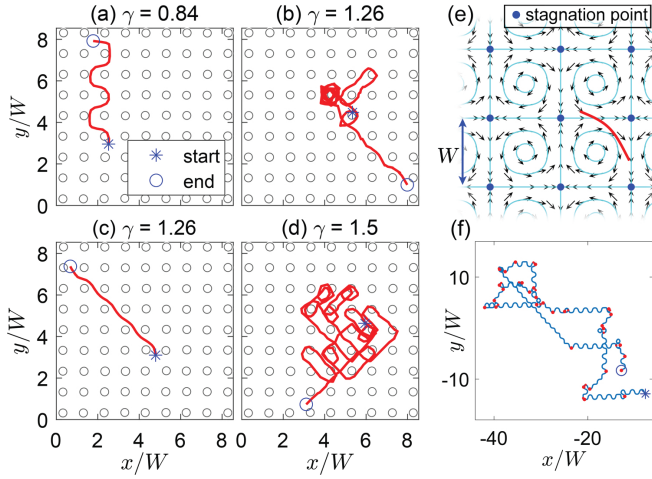
FIG. 1. Experimental COM trajectories of flexible ribbons in a 9-by-9 cellular flow, as shown on the left. Circles indicate the locations of the spinning rollers. (a) A strongly undulating step along $+y$ direction with $\eta \approx 25$. (b) A meandering trajectory with a long undulating diagonal step with $\eta \approx 85$. (c) Diagonal step with $\eta \approx 85$. (d) Meandering trajectory with many turns with $\eta \approx 118$. (e) Snapshot from a numerical simulation with $\eta = 100$ and $\gamma = 1$, showing a flexible filament moving in the cellular flow described by Eq. (1). Black arrows are the background cellular flow, and cyan closed curves are the streamlines. (f) A typical trajectory from simulation with $\gamma = 1$ and $\eta = 0.5$. The red points are turning points separating two different steps.

Motivating experiment.—We set up a cellular flow structure by immersing a square 9-by-9 roller array into a tank of pure glycerol (see Fig. 1 and details in Supplemental Material [33]). The rollers are interconnected and driven by a stepper motor. Through viscous coupling each roller rotates the fluid around it, with nearest neighbor rollers being counterrotating. Flexible ribbons, made from audio tape, are transported in the cellular flow and stay right beneath the fluid surface, resembling 2D motions. The effective flexibility $\eta \approx 7.5$–354. The Re $= \rho U_0 W / \mu \approx 0.1$ –1, where ρ is the density of glycerol. As shown in Fig. 1, a few interesting patterns of the ribbon's motion are identified. For moderate γ, despite occasional trappings, the ribbons can reach the edge of the cellular flow through undulating steps directed along diagonals or the $\pm x$ or $\pm y$ directions [Figs. 1(a)–1(c)]. However, for larger γ, the ribbons may meander around for a long time and make many turns before getting to the edge [Fig. 1(d)]. When η is sufficiently large, the ribbons are bent with large deformation and often trapped inside one of the fluid vortices.

Simulation and model.—As a model, we consider slender, inextensible, and elastic filaments of radius R and length L (with aspect ratio $\epsilon = R/L \ll 1$) moving in a Stokesian flow. Lengths are scaled on L, velocity on U_0, and time on L/U_0. The stream function Φ_γ of the background flow $\mathbf{U}$ is given by

$$\Phi_\gamma = (\pi\gamma)^{-1} \sin(\pi\gamma x) \sin(\pi\gamma y), \qquad (1)$$

which has stagnation points at $(n, m)\gamma^{-1}$ for n, m integers. The unit periodic cell is composed of four counterrotating vortices [Fig. 1(e)]. The filament centerline, denoted $\mathbf{r}(s, t)$, is parametrized by a signed arclength $s \in [-1/2, 1/2]$. From the leading-order slender body approximation [37], the centerline velocity $\mathbf{r}_t$ is governed by a local balance of drag force with the filament force (per unit length) upon the fluid,

$$\eta(\mathbf{I} - \mathbf{r}_s\mathbf{r}_s/2)(\mathbf{r}_t - \mathbf{U}[\mathbf{r}]) = -\mathbf{r}_{ssss} + (T\mathbf{r}_s)_s, \qquad (2)$$

where the effective flexibility $\eta = 8\pi\mu U_0 L^3/cB$ with $c = |\ln(\epsilon^2 e)|$, and $\mathbf{U}[\mathbf{r}]$ is the background flow along the filament centerline. The tensor $\mathbf{I} - \mathbf{r}_s\mathbf{r}_s/2$ captures the drag anisotropy of the filament. The filament force is described by Euler-Bernoulli elasticity: $\mathbf{f} = \mathbf{r}_{ssss} - (T\mathbf{r}_s)_s$, where determination of the tension T enforces filament inextensibility. Equation (2) is evolved numerically using a second-order finite difference method and implicit time stepping, while imposing zero-force and -torque boundary conditions [33].

The case of a rigid straight filament is informative [33]. We take $\mathbf{r}(s, t) = \mathbf{r}_c(t) + s\hat{\mathbf{p}}(t)$, where $\mathbf{r}_c$ is the COM position and $\hat{\mathbf{p}} = (\cos\theta_c, \sin\theta_c)$ with θ_c the filament orientation. Under zero-force and -torque conditions, the equations of motion are purely kinematic:

$$\dot{\mathbf{r}}_c = -\nabla^\perp_{\mathbf{r}_c} H \quad \text{with} \quad H = \int_{-1/2}^{1/2} \Phi_\gamma[\mathbf{r}(s, t)]ds, \quad (3)$$

$$\dot{\theta}_c = 12H - 6\{\Phi_\gamma[\mathbf{r}(1/2, t)] + \Phi_\gamma[\mathbf{r}(-1/2, t)]\}, \quad (4)$$

where $\nabla^\perp = (-\partial_y, \partial_x)$. In the "point limit" $\gamma = 0$, particle transport [Eq. (3)] is Hamiltonian, local, and decoupled from particle rotational dynamics. Increasing γ increases the averaging (over particle length) of the background flow, while also increasing the coupling of particle translation to rotation. This increase in system dimension leads to loss of integrability and allows for transport chaos. Equations (3) and (4) are evolved using a fourth-order Runge-Kutta scheme. Our simulations typically run for $2 \times 10^4 L/U_0$ to capture long-time dynamics.

Rigid filament simulations.—The filament COM trajectories show strong dependence on γ and the initial conditions. A common statistical measure of a complex trajectory is its step-length distribution $\phi(l)$ [38]. The step-length l is the straight-line distance between successive turning points, which separate two steps along different directions [see Fig. 1(f) and Supplemental Material in Ref. [33]]. For rigid filaments of different γ, Fig. 2(a) shows the complement of the cumulative distribution, $C(l) = 1 - \int_a^l \phi(l)dl$, for l in 400 trajectories with random initial conditions. We fit several random walk models using a maximum likelihood method [39,40]. At small γ, the best-fit models are mostly power laws given by $\phi(l) \propto l^{-(1+\beta)}$
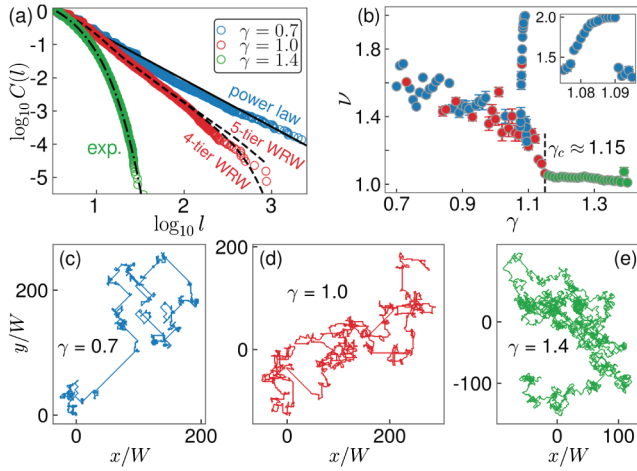
FIG. 2. From Lévy walks to Brownian walks for rigid filaments. Blue, power law $\phi(l)$; red, WRWs; and green, exponential $\phi(l)$. (a) $C(l)$ for $\gamma = 0.7$, 1.0, and 1.4, with best-fit distributions. With more statistics, higher-order terms in WRWs are needed [33]. (b) ν as a function of γ. Error bars represent uncertainties due to initial conditions. Inset: ν versus γ for $1.075 \leq \gamma \leq 1.095$. (c)–(e) Typical trajectories corresponding to the three cases shown in (a).

FIG. 3. (a) Lyapunov exponent λ as functions of γ for rigid filament. The large error bars for Lévy walks are due to the nonuniformity of the phase space. (b) $\mathrm{Var}(\mathbf{U}[\mathbf{r}])$ (left) and C_v (right) as a function of γ. (c)–(e) Maps of positive u_c (red, rightward motion) and negative u_c (blue, leftward motion) computed with $\theta_c = 3\pi/4$ (see text for details). Snapshots of the motion of rigid filaments are also shown with the time ordering labeled by numbers. Green thick lines trace the COM trajectories.

with $0 < \beta < 2$, indicating Lévy walks [38]. The trajectories show clusters of short steps interspersed with long steps [Fig. 2(c)]. At large γ, $\phi(l)$ fits well to exponential functions, and the filaments display Brownian walks [Fig. 2(e)]. At intermediate values of γ, with the exception of γ around 1.08–1.09, the best-fit models are mostly Weierstrassian random walks (WRW), which have been found in the studies of animal search strategies and random walks in bacterial swarms [18,41–43]. The $\phi(l)$ of the WRW is given by a hierarchical sum of exponential distributions with mean $b^{-(j+1)}$ weighted by $q^{-(j+1)}$: $\phi(l) \propto \sum_{j=0}^{J} q^{-(j+1)} b^{j+1} \exp(-b^{j+1}l)$, which resembles a power law when $J \to \infty$ and degenerates into an exponential distribution when $J = 0$.

The above transition through Lévy walks to Brownian walks is confirmed from the scaling exponent of mean squared displacement (MSD) [44], $\langle \delta^2(\tau) \rangle \sim \tau^\nu$ [Fig. 2(b)]. In general, ν decreases as γ increases. The critical γ separating the two transport behaviors is around 1.15. At γ around 1.08–1.09 [Fig. 2(b) inset], nearly ballistic trajectories are observed with $\nu \approx 2$. This is due to a geometric match of the filament length to the flow periodicity and is unstable under small perturbations of the flow field [33]. As shown in Fig. 3(a), the transition is accompanied by a growth in the Lyapunov exponent λ [33,45,46]: Brownian walks are more chaotic than Lévy walks. The phase space shows complex structures with strong dependence on γ, and Lévy walks are related to particle stickiness to regular islands [33]. A transition from Lévy walks to Brownian walks has been found in the transport of ions in optical lattice [47,48]. The presence of

Lévy walks is also known in Hamiltonian chaos, but the transitions are typically abrupt [49–52].

Mechanism.—We attribute the emergence of chaos and different random walks to the nonlocal geometrical averaging of the background flow by the filament from its broad extension across vortices. Considering rigid filament, from Eq. (3), the COM velocity of the filament is $\mathbf{v}_c = (u_c, v_c) = \int_{-1/2}^{1/2} \mathbf{U}[\mathbf{r}(s)]ds$. We first compute the variance of $\mathbf{U}[\mathbf{r}(s)]$: $\mathrm{Var}(\mathbf{U}[\mathbf{r}]) = \langle \int_{-(1/2)}^{(1/2)} \{ \mathbf{U}[\mathbf{r}(s)] - \mathbf{v}_c \}^2 ds \rangle$, where the average is taken with respect to $\mathbf{r}_c$ over the entire unit cell and θ_c over $[0, 2\pi)$. With the increase of γ [Fig. 3(b), left], $\mathrm{Var}(\mathbf{U}[\mathbf{r}])$ becomes larger, i.e., the background flow that the filament experienced on average becomes more variable. We also compute the correlation function between the unit velocity vectors of the filament's two ends ($s = 1/2, -1/2$): $C_v = \langle \hat{\mathbf{v}}(-1/2) \cdot \hat{\mathbf{v}}(1/2) \rangle$, where the average is along COM trajectories [Fig. 3(b), right]. When C_v is large, the filament is likely to be translated along a flow but to be turned around when C_v is small. Both $\mathrm{Var}(\mathbf{U}[\mathbf{r}])$ (increasing with γ) and C_v (decreasing with γ) show that long filaments with large γ can hardly travel long unidirectional steps but rather turn around and take seemingly random and diffusive motions. On the other extreme at very small γ, filaments are too short to perceive any flows outside the local circulation within which it resides, and most of the filaments are trapped except those initially close to the separatrices. Therefore, the only possible long-distance travelers are those filaments of intermediate lengths.

Indeed, we find some clues by mapping the spatial distributions of x-component COM velocity $u_c(\mathbf{r}_c, \theta_c)$. In Figs. 3(c)–3(e), the maps of u_c were made with $\theta_c = 3\pi/4$, but any other values of θ_c in the second and fourth quadrants would result in similar maps but a slightly smaller magnitude of u_c. When $\gamma \ll 1$ [Fig. 3(c)], areas of positive u_c values (red, rightward motion) and negative u_c values (blue, leftward motion) are isolated from each other, and filament cannot travel across vortices. As γ increases, the red and blue regions start to deform and morph into many alternating "conveyor belts" flowing toward opposite directions [Figs. 3(d) and 3(e)]. If θ_c lies in the first and third quadrants, the conveyor belts will take the other diagonals oriented $\pi/2$ from those in Figs. 3(d) and 3(e). The filament can now move across vortices and travel long steps. We see two competing effects at work as γ further increases: longer filament promotes the formation of conveyor belts, but at the same time it is more likely to turn and change directions. The latter effect is demonstrated in Fig. 3(e) as a long filament is captured first by an opposite conveyor belt (label 4) and then turns (label 5) with its two ends moving oppositely.

The patterns of filament dispersal at scales much larger than W are significantly different for different random walks. For those performing Lévy walks they are strikingly anisotropic. Figure 4(a) shows that for $\gamma = 0.7$, the probability density function (PDF) $P(\mathbf{x}, t)$ of finding a filament at position $\mathbf{x}$ at time t after starting off with random initial conditions from the unit cell centered at the origin has a 4-pointed star-like structure with four branches extending along the diagonals specified by $(\hat{d}_1, \hat{d}_2)$. Such anisotropy arises from the long unidirectional diagonal steps due to the conveyor belts. In particular, a sharp peak exists at the far front of each branch [Fig. 4(b)] reflecting the microscopic geometry of the Lévy walks [53]: filaments can only move
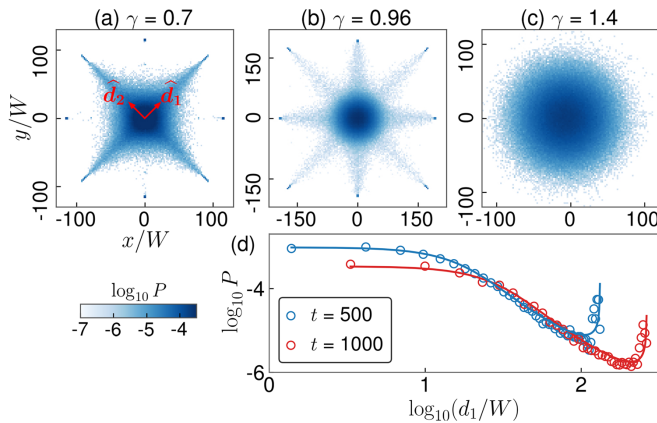
along $\hat{d}_1$ or $\hat{d}_2$ at each step. The PDF along $\hat{d}_1$ is given by a product of a 1D Lévy distribution and a prefactor that accounts for the decrease in the spread of the PDF along $\hat{d}_2$ [53],

$$P(d_1, t) \propto [1 - d_1/(ct)]^{-1/\beta} L_\beta^\sigma(d_1), \tag{5}$$

where c is the average speed of the filaments and L_β^σ is a 1D Lévy distribution with exponent β and scale parameter σ ($\propto t^{1/\beta}$). Equation (5) agrees well with the simulation result [Fig. 4(d)]. As γ increases, undulating steps along $\pm x$ or $\pm y$ directions become more frequent, and 8-pointed star-like patterns are formed [Fig. 4(b)]. While almost unapparent, these additional branches can be faintly discerned in Fig. 4(a). Eventually in the Brownian-walk regime for sufficient large γ, in sharp contrast to Lévy walks, the PDF follows an isotropic 2D Gaussian distribution with its variance scaling linearly with time t [Fig. 4(c)].

Flexible filament simulations.—By extensively surveying the phase space of γ and η, for the first time, we construct a phase diagram showing various transport states [see Fig. 5(a) and Supplemental Material in Ref. [33]]. Highly flexible filaments ($\eta \gtrsim 10^2$) are deformed and trapped inside vortices for all values of γ, as is also observed in the experiments. For relatively rigid filaments ($\eta \lesssim 10$), the transport states are determined by γ. The boundary that separates Lévy walks ($1 < \nu < 2$) and Brownian walks ($\nu \approx 1$) is located around $\gamma = 1.15$. At intermediate η between 10–10^2, the filament first meanders around for a short period before moving indefinitely along diagonals or $\pm x$ and $\pm y$ directions. We call this type of transport behavior a ballistic state with $\nu \approx 2$. Even within the ballistic state, the filament dispersal patterns show strong dependence on both γ and η, and filaments with

FIG. 4. Dispersal patterns of 10^6 rigid filaments. PDF $P(x, y)$ at $t = 500$ for (a) $\gamma = 0.7$, (b) $\gamma = 0.96$, and (c) $\gamma = 1.4$. (d) PDF along direction $\hat{d}_1$ shown in (a) at two different time instants for $\gamma = 0.7$. Solid lines are the fittings of the theoretical result given by Eq. (5).
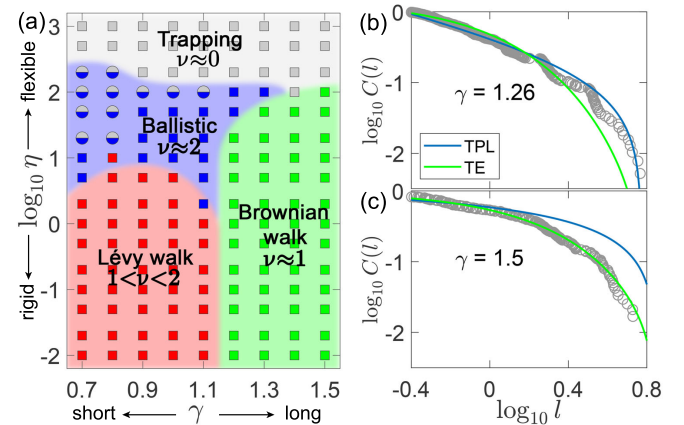
FIG. 5. (a) From simulation, the phase diagram of the transport states constructed using MSD. Depending on the initial conditions, ballistic states may coexist with trapping states (circles). (b),(c) $C(l)$ from 52 trajectories in experiments for two different values of γ.

different lengths and flexibility are dynamically sorted [33]. The dispersal rate of filaments is largest in the ballistic state, followed by Lévy walks and then Brownian walks. There is no long-range transport in the trapping state.

Experimental evidence.—We find evidence that shorter ribbons perform Lévy walks while longer ribbons perform Brownian walks in the experiments [33]. Figures 5(b) and 5(c) show two examples. For $\gamma = 1.26$, the best-fit model is the truncated power law (TPL) [54] supporting a Lévy walk; for $\gamma = 1.5$, the step-length distribution better resembles a truncated exponential (TE) model supporting a Brownian walk. The γ value that separates the two states is estimated to be around 1.4, which differs from the value found in the simulation. This discrepancy is possibly caused by the presence of the roller boundaries. Despite the subtle difference in $C(l)$ due to the limited size of the flow field in the experiments, the trajectories for the two states are significantly different from each other as depicted in Fig. 1: with more turns in the trajectories, longer ribbons take a much longer time to reach the edge of the flow field than shorter ribbons. Our experiments on the effect of η are limited, but for large η, the ribbon is typically bent around one of the rollers and trapped for a long time.

Discussion.—Our experiments and simulations demonstrate that this simple system of semirigid filaments moving in Stokesian cellular vortical flows has a surprisingly rich range of dispersal dynamics, including Lévy walks and path chaos. For $\gamma \gg 1$ our limited simulations show mostly Brownian walks due to averaging over multiple vortices. The emergence of cross-vortex motion and chaos in our system does not require the flow itself to be time dependent and chaotic as it does for tracer particles [17,55]. It arises from the elongated body being able to broadly sample the background vortical field, and the strong coupling of rotational to translational dynamics afforded by that elongation. The cross-streamline motion and escape from local flows shown by the semirigid filaments have implications for efficient fluid mixing at low Re by additives [8,56]. Similar to the billiards system [29,30], the anisotropic dispersals of filaments in the Lévy-walk state and ballistic state are also originated from long unidirectional steps preprogrammed by the fundamental geometries of the backgrounds. However, the dominant directions of motion depend on the relative length γ and effective flexibility η of filaments in our system but are fully specified by the geometries of scatterers in the billiards. Most prominently, various transport states can be achieved by tuning different length scales, which also serves as the underlying mechanism of gel electrophoresis [57]. Our results may open up new possibilities for efficient dynamical sorting of elongated particles and semiflexible biopolymers [57–60].

---

[*]shelley@cims.nyu.edu
[†]jun@cims.nyu.edu

[1] A. D. Stroock, S. K. W. Dertinger, A. Ajdari, I. Mezić, H. A. Stone, and G. M. Whitesides, Science **295**, 647 (2002).

[2] A. Groisman and V. Steinberg, Nature (London) **405**, 53 (2000).

[3] P. E. Arratia, C. C. Thomas, J. Diorio, and J. P. Gollub, Phys. Rev. Lett. **96**, 144502 (2006).

[4] V. Steinberg, Annu. Rev. Fluid Mech. **53**, 27 (2021).

[5] D. J. Pine, J. P. Gollub, J. F. Brady, and A. M. Leshansky, Nature (London) **438**, 997 (2005).

[6] C. Dombrowski, L. Cisneros, S. Chatkaew, R. E. Goldstein, and J. O. Kessler, Phys. Rev. Lett. **93**, 098103 (2004).

[7] D. Saintillan and M. J. Shelley, C.R. Phys. **14**, 497 (2013).

[8] A. Groisman and V. Steinberg, Nature (London) **410**, 905 (2001).

[9] H. A. Stone, A. D. Stroock, and A. Ajdari, Annu. Rev. Fluid Mech. **36**, 381 (2004).

[10] C.-Y. Lee, C.-L. Chang, Y.-N. Wang, and L.-M. Fu, Int. J. Mol. Sci. **12**, 3263 (2012).

[11] K. Ward and Z H. Fan, J. Micromech. Microeng. **25**, 094001 (2015).

[12] J. Nam, H. Lim, D. Kim, H. Jung, and S. Shin, Lab Chip **12**, 1347 (2012).

[13] S. Yazdi and A. M. Ardekani, Biomicrofluidics **6**, 044114 (2012).

[14] A. Karimi, S. Yazdi, and A. M. Ardekani, Biomicrofluidics **7**, 021501 (2013).

[15] X. Lu, C. Liu, G. Hu, and X. Xuan, J. Colloid Interface Sci. **500**, 182 (2017).

[16] H. Stommel, J. Mar. Res. **8**, 24 (1949).

[17] T. H. Solomon and J. P. Gollub, Phys. Rev. A **38**, 6280 (1988).

[18] G. Ariel, A. Be'er, and A. Reynolds, Phys. Rev. Lett. **118**, 228102 (2017).

[19] D. Rothstein, E. Henry, and J. P. Gollub, Nature (London) **401**, 770 (1999).

[20] N. T. Ouellette and J. P. Gollub, Phys. Rev. Lett. **99**, 194502 (2007).

[21] E. Wandersman, N. Quennouz, M. Fermigier, A. Lindner, and O. du Roure, Soft Matter **6**, 5715 (2010).

[22] C. Torney and Z. Neufeld, Phys. Rev. Lett. **99**, 078101 (2007).

[23] G. Ariel, A. Rabani, S. Benisty, J. D. Partridge, R. M. Harshey, and A. Be'er, Nat. Commun. **6**, 8396 (2015).

[24] G. Ariel and J. Schiff, Physica (Amsterdam) **411D**, 132584 (2020).

[25] J. LaGrone, R. Cortez, W. Yan, and L. Fauci, J. Non-newton Fluid Mech. **269**, 73 (2019).

[26] Y.-N. Young and M. J. Shelley, Phys. Rev. Lett. **99**, 058303 (2007).

[27] N. Quennouz, M. Shelley, O. du Roure, and A. Lindner, J. Fluid Mech. **769**, 387 (2015).

[28] O. du Roure, A. Lindner, E. Nazockdast, and M. J. Shelley, Annu. Rev. Fluid Mech. **51**, 539 (2019).

[29] L. Zarfaty, A. Peletskyi, I. Fouxon, S. Denisov, and E. Barkai, Phys. Rev. E **98**, 010101(R) (2018).

[30] L. Zarfaty, A. Peletskyi, E. Barkai, and S. Denisov, Phys. Rev. E **100**, 042140 (2019).

[31] R. Klages, Sol Selene Gil Gallegos, J. Solanpää, M. Sarvilahti, and E. Räsänen, Phys. Rev. Lett. **122**, 064102 (2019).

[32] C. H. Wiggins and R. E. Goldstein, Phys. Rev. Lett. **80**, 3879 (1998).

[33] See Supplemental Material at http://link.aps.org/supplemental/10.1103/PhysRevLett.127.074503 for videos, experimental and simulation details, data analysis, and dispersal patterns, which includes Refs. [34–36].

[34] A. K. Tornberg and M. J. Shelley, J. Comput. Phys. **196**, 8 (2004).

[35] J. A. G. Roberts and G. R. W. Quispel, Phys. Rep. **216**, 63 (1992).

[36] K. P. Burnham and D. R. Anderson, *Model Selection and Multimodel Inference: A Practical Information-Theoretic Approach* (Springer-Verlag, New York, USA, 2002).

[37] J. B. Keller and S. I. Rubinow, J. Fluid Mech. **75**, 705 (1976).

[38] V. Zaburdaev, S. Denisov, and J. Klafter, Rev. Mod. Phys. **87**, 483 (2015).

[39] A. Edwards *et al.*, Nature (London) **449**, 1044 (2007).

[40] A. Clauset, C. R. Shalizi, and M. E. J. Newman, SIAM Rev. **51**, 661 (2009).

[41] B. D. Hughes, M. F. Shlesinger, and E. W. Montroll, Proc. Natl. Acad. Sci. U.S.A. **78**, 3287 (1981).

[42] A. M. Reynolds, P. Schultheiss, and K. Cheng, J. Theor. Biol. **340**, 17 (2014).

[43] A. M. Reynolds, Sci. Rep. **4**, 4409 (2015).

[44] R. Metzler, J.-H. Jeon, A. G. Cherstvy, and E. Barkai, Phys. Chem. Chem. Phys. **16**, 24128 (2014).

[45] G. Benettin, L. Galgani, A. Giorgilli, and J. M. Strelcyn, Meccanica **15**, 9 (1980).

[46] K. Ramasubramanian and M. S. Sriram, Physica (Amsterdam) **139D**, 72 (2000).

[47] S. Marksteiner, K. Ellinger, and P. Zoller, Phys. Rev. A **53**, 3409 (1996).

[48] H. Katori, S. Schlipf, and H. Walther, Phys. Rev. Lett. **79**, 2221 (1997).

[49] A. A. Chernikov, B. A. Petrovichev, A. V. Rogal'sky, R. Z. Sagdeev, and G. M. Zaslavsky, Phys. Lett. A **144**, 127 (1990).

[50] G. M. Zaslavsky, D. Stevens, and H. Weitzner, Phys. Rev. E **48**, 1683 (1993).

[51] S. Benkadda, S. Kassibrakis, R. B. White, and G. M. Zaslavsky, Phys. Rev. E **55**, 4909 (1997).

[52] M. Harsoula and G. Contopoulos, Phys. Rev. E **97**, 022215 (2018).

[53] V. Zaburdaev, I. Fouxon, S. Denisov, and E. Barkai, Phys. Rev. Lett. **117**, 270601 (2016).

[54] D. A. Raichlen, B. M. Wood, A. D. Gordon, A. Z. P. Mabulla, F. W. Marlowe, and H. Pontzer, Proc. Natl. Acad. Sci. U.S.A. **111**, 728 (2014).

[55] T. H. Solomon, E. R. Weeks, and H. L. Swinney, Phys. Rev. Lett. **71**, 3975 (1993).

[56] S. H. Lee, D. van Noort, J. Y. Lee, B.-T. Zhang, and T. H. Park, Lab Chip **9**, 479 (2009).

[57] K. D. Dorfman, S. B. King, D. W. Olson, J. D. P. Thomas, and D. R. Tree, Chem. Rev. **113**, 2584 (2013).

[58] L. R. Huang, J. O. Tegenfeldt, J. J. Kraeft, J. C. Sturm, R. H. Austin, and E. C. Cox, Nat. Biotechnol. **20**, 1048 (2002).

[59] P. Sajeesh and A. K. Sen, Microfluid. Nanofluid. **17**, 1 (2014).

[60] B. Chakrabarti, C. Gaillard, and D. Saintillan, Soft Matter **16**, 5534 (2020).